

NO-A176 151

A NUMERICAL STUDY OF FLARE STABILIZED PROJECTILES AT
MACH 70(U) AIR FORCE ARMAMENT LAB EGLIN AFB FL
M C HUGHSON ET AL 87 JAN 87 AFATL-TR-87-01

1/1

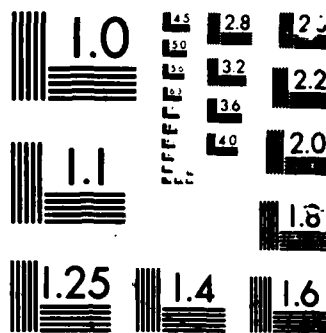
UNCLASSIFIED

SBI-AD-E801 439

F/G 20/4

NL





REPORT DOCUMENTATION PAGE

1a. REPORT SECURITY CLASSIFICATION Unclassified		DTIC ELECTED JAN 13 1987		1b. RESTRICTIVE MARKINGS	
2a. SECURITY CLASSIFICATION AUTHORITY N/A		3. DISTRIBUTION / AVAILABILITY OF REPORT Approved for public release; distribution is unlimited.		5. MONITORING ORGANIZATION REPORT NUMBER(S) AFATL-TR-87-01	
2b. DECLASSIFICATION / DOWNGRADING SCHEDULE N/A		4. PERFORMING ORGANIZATION REPORT NUMBER(S)		6a. NAME OF PERFORMING ORGANIZATION Air Force Armament Laboratory Aerodynamics Branch	
6c. ADDRESS (City, State, and ZIP Code) Eglin AFB FL 32542-5434		6b. OFFICE SYMBOL (if applicable) AFATL/FXA		7a. NAME OF MONITORING ORGANIZATION Air Force Armament Laboratory Aeromechanics Division	
8a. NAME OF FUNDING / SPONSORING ORGANIZATION N/A		8b. OFFICE SYMBOL (if applicable)		7b. ADDRESS (City, State, and ZIP Code) Eglin AFB FL 32542-5434	
8c. ADDRESS (City, State, and ZIP Code) N/A		9. PROCUREMENT INSTRUMENT IDENTIFICATION NUMBER N/A		10. SOURCE OF FUNDING NUMBERS	
		PROGRAM ELEMENT NO 62602F	PROJECT NO. 2567	TASK NO. 03	WORK UNIT ACCESSION NO. 10
11. TITLE (Include Security Classification) A Numerical Study of Flare Stabilized Projectiles at Mach 7.0					
12. PERSONAL AUTHOR(S) Montgomery C. Hughson, Gary T. Chapman					
13a. TYPE OF REPORT Final		13b. TIME COVERED FROM Oct 85 TO Jan 87		14. DATE OF REPORT (Year, Month, Day) January 7, 1987	
15. PAGE COUNT 8					
16. SUPPLEMENTARY NOTATION None					
17. COSATI CODES			18. SUBJECT TERMS (Continue on reverse if necessary and identify by block number)		
FIELD 01	GROUP 01	SUB-GROUP	Parabolized Navier-Stokes Code Hypervelocity Projectiles		
19. ABSTRACT (Continue on reverse if necessary and identify by block number) The effect of nose shape on two flare stabilized projectiles was studied using a Parabolized Navier-Stokes code. Pressure coefficients, forces and moments, skin friction coefficients, and Stanton number calculations are presented for the hemisphere-cylinder-flare and the cone-cylinder-flare configurations. Pitching moment and static margin plots versus flare angles and flare lengths are presented in a parametric study to show aerodynamic stability effects. Distinctly different flow field values of pressure, local Mach number, and dynamic pressure were generated by the two different nose configurations. These flow field values just upstream of the flare will be examined. The code demonstrated its value as a design tool by making a clear distinction between aerodynamically stable characteristics for this variety of nose shapes, flare angles, and flare lengths.					
20. DISTRIBUTION / AVAILABILITY OF ABSTRACT <input type="checkbox"/> UNCLASSIFIED/UNLIMITED <input checked="" type="checkbox"/> SAME AS RPT <input type="checkbox"/> DTIC USERS			21. ABSTRACT SECURITY CLASSIFICATION Unclassified		
22a. NAME OF RESPONSIBLE INDIVIDUAL Montgomery C. Hughson			22b. TELEPHONE (Include Area Code) (904) 882-3124		22c. OFFICE SYMBOL FXA

**A NUMERICAL STUDY OF FLARE STABILIZED PROJECTILES
AT MACH 7.0**

Montgomery C. Hughson*
U.S. Air Force Armament Laboratory
Eglin Air Force Base, FL 32542-5434

Gary T. Chapman**
NASA Ames Research Center
Moffett Field, CA 94035

Abstract

The effect of nose shape on two flare stabilized projectiles was studied using a Parabolized Navier-Stokes code. Pressure coefficients, forces and moments, skin friction coefficients, and Stanton number calculations are presented for the hemisphere-cylinder-flare and the cone-cylinder-flare configurations. Pitching moment and static margin plots versus flare angles and flare lengths are presented in a parametric study to show aerodynamic stability effects. Distinctly different flow field values of pressure, local Mach number, and dynamic pressure were generated by the two different nose configurations. These flow field values just upstream of the flare will be examined. The code demonstrated its value as a design tool by making a clear distinction between aerodynamically stable characteristics for this variety of nose shapes, flare angles, and flare lengths.

Introduction

The stabilizing effect of flared afterbodies has long been incorporated in the design of rockets and projectiles. For short projectiles at relatively high Mach numbers, the flare angle and the flare length can play a significant role in the projectile's aerodynamic stability. Extensive experimental studies have been made on cone-cylinder-flared projectiles at Mach numbers ranging from 2 to 4¹⁻³ and a Parabolized Navier-Stokes (PNS) code has been used for numerical studies.^{4,5} Most of these studies involved conical nosed bodies at lower supersonic speeds.

This paper will present aerodynamic characteristics determined numerically for two flare stabilized configurations at Mach 7 and at 2° angle of attack; a hemisphere-cylinder-flare and a cone-cylinder-flare. Mach 7 was chosen because it was high enough to yield characteristically high Mach number effects yet low enough that real gas effects can be ignored. The low angle of attack was selected to generate pitching moment data. The effect of the nose shape on each

projectile's aerodynamic stability will be considered. Within that context, the flare angle and the flare length will be varied to study the effect of these two parameters. A brief description of the PNS code, code inputs, configurations, and flow conditions will be presented in the second section. Aerodynamic results will be compared for each configuration in the third section. Finally, conclusions to be drawn will be presented in the last section.

PNS Code and Configurations

A Parabolized Navier-Stokes code⁶ used for this numerical study generates finite difference approximations to steady, three-dimensional solutions of supersonic flow over arbitrarily shaped bodies at high Reynolds number as long as there are no large subsonic or axially separated regions. From an initial condition starting solution, the code marches downstream from any given axial location on the body. For the blunt hemispherical nose configuration in Figure 1(a), the code needed an input starting solution obtained from a thin-layer unsteady Navier-Stokes code.⁷ For the sharp conical nose configuration in Figure 1(b), the PNS code has a self-start capability wherein initial starting planes are calculated within the code.

The PNS code is a space marching code which uses a numerical method originally developed at NASA Ames Research Center by Schiff and Steger.⁸ This technique obtains finite difference solutions by solving implicit difference equations noniteratively by way of local linearization of the flux vector. The resulting system of algebraic equations are solved using the Beam-Warming method⁹ of implementing the alternating direction implicit scheme using the delta formulation. Several additional modifications to the code have been made.¹⁰⁻¹³

The PNS flow field predictions for the hemisphere-cylinder-flare were obtained by marching from a starting solution generated by a thin-layer unsteady Navier-Stokes code.⁷ This starting solution was obtained at an axial location at the hemisphere-cylinder shoulder with an algebraic grid of 19 by 30 points in the circumferential and radial directions, respectively. This data was then interpolated to obtain an algebraic grid of 19 by 45 points. The data was obtained at 0° angle of attack and then rotated to a 2° angle of attack. For a hemispherical nose, this rotation presents no problems theoretically. Thirty-five of the 45 radial grid points were clustered near the wall to resolve the boundary layer. A marching step size

* 2Lt, Aerospace Engineer, Aeromechanics Division
Member AIAA

**Senior Staff Scientist, Thermosciences Division
Senior Member AIAA

of 0.01 cylinder diameters was used up to a location one-half cylinder diameter aft of the hemisphere-cylinder shoulder. This small step size captured the strong gradients in the flow field in this shoulder region. The step size was then increased to 0.03 diameters for marching along the cylinder to a plane 0.13 diameters upstream of the cylinder-flare juncture. A reduced step size of 0.02 diameters was used to adjust for the rapid pressure rise in the region at the flare. This step size was close to one-third the boundary layer thickness predicted by the PNS code at this point. Analysis by Viegas and Horstman indicate that a step size one-half the boundary layer thickness is sufficient to resolve two-dimensional shock/boundary layer interactions.¹⁴ Calculations were made on 0, 5, 10, 15, 20, and 25 degree flare angles. Attempts to calculate a 30° flare angle failed with axial flow separation characteristics. This is consistent with the PNS code's ability to detect the onset of incipient separation as evaluated by Cottrell and Chapman.⁴ This failure may also be attributed to the Beam-Warming type of algorithm which tends to introduce errors in the form of local flow property oscillations as a result of the central-differencing of fluxes across discontinuities.¹⁵ Versions of the PNS code using an upwind-differencing scheme to alleviate this problem are being employed. The code's smoothing terms were as follows: explicit damping parameter of 0.2, implicit damping parameter of 0.4, stability coefficients of 0.25. The nominal value of the grid spacing at the wall was 0.5×10^{-5} .

The PNS flow field prediction for the cone-cylinder-flare configuration was obtained by marching from a solution generated by the code's self-start option for sharp conical noses. This starting solution was obtained at an axial location 1 cylinder diameter from the nosetip at a 2° angle of attack. The algebraic grid was 19 by 45 points in the circumferential and radial directions, respectively. Thirty-five of the 45 radial grid points were clustered near the wall to resolve the boundary layer. This grid is set up exactly the same as the grid for the hemisphere-cylinder-flare. However, the volume of the grid for the cone-cylinder-flare case is much smaller than the volume of the grid for the hemisphere-cylinder-flare case due to the smaller distance of the bow shock. Hence, the grid points clustered near the wall for the cone-cylinder-flare are packed closer together. A marching step size of 0.02 diameters was used to a plane 0.8 cylinder diameters aft of the cone-cylinder shoulder. This small step size resolved the large gradients in the flow field as the solution marched up over the shoulder. The step size was then increased to 0.04 diameters for marching along the cylinder to a plane 0.14 diameters upstream of the cylinder-flare juncture. The step size was reduced back down to 0.02 diameters to adequately resolve the rapid pressure rise in the flare region. For the 20° flare, the step size was kept at 0.04 diameters. A flare angle of 25° was attempted but the code indicated the onset of axial flow separation just as the 30° flare angle attempt for the hemisphere-cylinder-flare did and the reasons cited at that time are applicable here, also. The smoothing terms were kept the same as those used in the hemisphere-cylinder-flare study for all cases.

Results and Discussion

Hemisphere-Cylinder-Flare

Figure 2 shows the shock structure for the hemisphere-cylinder-15 degree flare at Mach 7. The outer boundary shock was fit by the unsteady Navier-Stokes code for the hemisphere nose segment and the PNS code fit the shock for the cylinder-flare segment. Note the small discontinuity where the shock fits are joined together at the shoulder region. This is not unusual when shifting from an unsteady Navier-Stokes code to a PNS code. The unsteady code captured the subsonic region of the nose. The sonic lines were estimated from locations where the total Mach equaled 1. The embedded secondary shock locations were captured by the PNS code and the estimated locations in the flare region were obtained from P/P_{inf} distributions between the body and the shock at the leeward and at the windward planes. These captured shocks are smeared across grid points and sharp discontinuities are not apparent. Figure 3 shows pressure coefficient distributions at the surface at three circumferential stations: a windward ray, a 90° or side ray, and a leeward ray. As anticipated at this small angle of attack, there is a slightly larger C_p on the windward side which decreases slowly as one moves circumferentially to the lower C_p on the leeward side. From a C_p of 1.83 at the nose stagnation point, the flow field pressure undergoes a rapid expansion over the nose shoulder, decreases gradually along the cylinder body, and jumps quickly at the cylinder-flare juncture. Note once again that the joining of unsteady Navier-Stokes code data with PNS code data results in a slight C_p discontinuity in the shoulder region. Figures 4-6 show pressure coefficient distributions at the same three circumferential stations on the cylinder-flare segment for flare angles at 0 and 15, 5 and 20, and 10 and 25 degrees. Note how the pressure jumps at the cylinder-flare juncture. For lower flare angles, the pressure jumps and then decays as expected for uniform flow approaching the flare (i.e., jump to pressure associated with a 2-D wedge and then drop down to pressure associated with a cone). At the 20 and 25 degree flare angles, there appears a deviation from this trend. This is due to nonuniform flow approaching the flare and will be discussed further in the comparison with the cone-cylinder case. Attempts to calculate a 30° flare case failed with axial flow separation characteristics for reasons discussed earlier.

It should be noted that this marching code cannot predict the pressures on the base of the flare. If the pressure distribution on the base is uniform, then the base pressure effect on pitching moment is negligible for this small angle of attack. Pitching moment curves versus flare lengths for various flare angles are shown in Figure 7. Stability grows with increases in both flare length and flare angle. These results are similar to the stability trends reported by Cottrell and Chapman.⁴

Static margin curves were constructed by subtracting the center of gravity (cg) location from the center of pressure location. A homogeneous body was assumed for the cg calculation. The center of pressure locations

CHIEF INSPECTOR
4

1000

ES

were calculated by the PNS code. Both locations were measured positively from the nose. When the center of pressure is farther away from the nose than the cg, the nose will pitch downward which indicates aerodynamic stability. In Figure 8, the static margin for 0, 5, 10, 15, 20, and 25 degree flare angles is plotted for various flare lengths. For the 0, 5, and 10 degree flare cases, these curves indicate unstable aerodynamics for whatever flare length chosen. The 10° flare indicates an impasse where an increase in flare length moves the cg and the center of pressure the same distance with no further stability deterioration or increase. Note that the 15, 20, and 25 degree flare cases go stable rather quickly with increasing flare angle and flare length in a manner similar to that reported by Cottrell and Chapman.⁴ These last three flare angles all go stable for flare lengths over one-third cylinder diameter long.

Figures 9 and 10 show typical skin friction coefficient and heat transfer (Stanton number) distributions. In Figure 9, skin friction decays smoothly with axial position except near the cylinder-flare juncture. The expansion of the flow at the cone-cylinder shoulder increases the boundary layer thickness resulting in a rapid decrease in skin friction coefficient which steadies to a smooth decay down the cylinder segment. The spike in the skin friction coefficient at the cylinder-flare juncture is physically unreal. It may be attributed to the nature of the PNS type of algorithm. In Figure 10, Stanton number, or heat transfer, also decreases smoothly with axial position except near the cylinder-flare juncture. The spike at that juncture is physically unreal.

Cone-Cylinder-Flare

Figure 11 shows the shock structure for the cone-cylinder-15 degree flare at Mach 7. The attached shock at the nose and the outer shock location were estimated by the PNS code in the step-back mode up to a location one cylinder diameter from the nosetip. Planes of data were stored there. The PNS code picked this data up and marched down the rest of the configuration. Once again, the estimated embedded shock locations on the flare were approximated from the P/P_{inf} distributions between the body and shock at the windward and leeward planes. Figure 12 shows pressure coefficient distributions along the configuration at the surface for the 15° flare case. Note the Prandtl - Meyer expansion at the cone-cylinder shoulder which drops pressure rapidly from a stagnation C_p of 2.13. Then there is a gradual expansion back to near freestream pressure values down the cylinder segment. Figures 13-15 show pressure coefficient distributions on the cylinder-flare segment for flare angles of 0 and 15, 5 and 20, and 10 degrees. Note how the pressure data jumps at the cylinder-flare juncture for all cases followed by a continual pressure rise normally associated with nonuniform flow. This nonuniform aspect of the flow will be discussed in the comparison section that follows. Attempts to calculate a 25° flare failed with axial flow separation characteristics consistent with the results found by Cottrell and Chapman⁴ but may also be attributed to the Beam-Warming algorithm mentioned previously. Pitching

moment curves versus flare lengths for various flare angles are shown in Figure 16. As expected, the pitching moment grows as flare angle and flare length increases.

Static margin curves were constructed from the PNS code data and are shown for flare angles 0, 5, 10, 15, and 20 degrees in Figure 17. Note it appears that the 0 and 5 degree flare angles will never yield aerodynamic stability by increasing the flare length. Note, too, that the 10° flare goes stable at a flare length approximately one-third cylinder diameter. The 15 and 20 degree flares yield stability rather quickly as the flare length increases.

Figures 18 and 19 show skin friction coefficient and heat transfer (Stanton number) distributions. The spike at the flare for both of these plots is not realistic and may be attributed to flow property oscillation problems mentioned earlier.

Comparison of Configuration Results

A comparison of the aerodynamic results must start with an examination of the outer shock boundaries in Figures 2 and 11. The hemisphere nose generates a detached bow shock with a characteristic subsonic region while the cone nose has an attached shock. The difference between these bow shock waves lead to very different flow conditions in front of the flares. Figures 20, 21, and 22 show the radial distribution of P/P_{inf} , local Mach number, and dynamic pressure (q/q_{inf}), respectively. These distributions are taken at a location just upstream of the cylinder-flare juncture for the hemisphere-cylinder-flare and for the cone-cylinder-flare configurations. Also shown in these figures are the effective height of a 10° and a 20° flare at the base. This gives a rough idea of the flow encountered by these flares. Figures 23(a) and 23(b) show the algebraic grid at these locations for the hemisphere-cylinder-flare and for the cone-cylinder-flare, respectively.

The P/P_{inf} plot in Figure 20 reveals the large region of constant pressure each configuration has. Pressures just before the flare are close to 50% higher for the hemispherical nose configuration. The strong bow shocks on each of the two lead to significant entropy losses. The blunt hemisphere body has the greater losses. This is illustrated by the lower local Mach number and the lower dynamic pressure in front of the flare for this blunt nose compared to the cone nose as shown in Figures 21 and 22. The significant reduction in dynamic pressure accounts for the much lower static margins of the hemisphere-cylinder-flare compared to the cone-cylinder-flare configuration.

Although the hemispherical nosed body has the greater entropy losses of the two, the conical nosed body has more of a variation in local Mach number radially over the distance comparable to the flare height. It is this variation that accounts for the rather smooth pressure coefficient rise along the flare on the conical-nosed body seen in Figures 12-15. This variation in local Mach number is only present in a small radial region for the hemispherical-nose body. Hence, only the smaller flare angles for the

hemispherical-nose body have smooth pressure rises on the flare as seen in Figures 3-6.

Concluding Remarks

Based on the predictions made with the PNS code on the hemisphere-cylinder-flare at various flare angles and flare lengths with flow conditions of Mach 7 and at 2° angle of attack, the following conclusions can be drawn.

At this hypersonic speed, the nose shape has a distinct effect on the aerodynamic stabilizing effect of flared afterbodies. Of the two configurations examined, the conical-nosed body has greater stability and, therefore, more utility at hypersonic applications. It appears an attached shock will keep entropy losses to a minimum. This provides the stabilizing control surfaces within the outer shock enveloping the body a more effective role in the projectile's hypersonic mission. Furthermore, the increased stability obtained at larger flare angles and greater flare lengths for both configurations have been presented.

References

1. Sims, J.L. and Henderson, J.H., "Normal Force, Pitching Moment, and Center of Pressure of Eighty Cone-Cylinder-Frustum Bodies of Revolution at Mach Number 2.81," Department of the Army Ordnance Corps Report No. 6R3N2, Redstone Arsenal, March 1956.
2. Henderson, J.H. and Sims, J.L., "Normal Force, Pitching Moment, and Center of Pressure of Eighty Cone-Cylinder-Frustum Bodies of Revolution at Mach Number 4.04," Department of the Army Ordnance Corps Report No. 6R3N1, Redstone Arsenal, March 1956.
3. Lavender, R.E., Henderson, J.H., and Deep, R.A., "Normal Force, Pitching Moment, and Center of Pressure of Eighty Cone-Cylinder-Frustum Bodies of Revolution at Mach Number 2.18," Department of the Army Ordnance Corps Report No. 6R3P, Redstone Arsenal, July 1956.
4. Cottrell, C.J. and Chapman, G.T., "An Evaluation of a Parabolized Navier-Stokes (PNS) Code for Cone-Cylinder-Flared Configurations," AIAA Paper 84-2116, Seattle, WA, August 1984.
5. Cottrell, C.J., Chapman, G.T., and Roth, K.R., "A Numerical Investigation of the Aerodynamics of Biconic and Non-Circular Flared Configurations," AIAA Paper 85-1814, Snowmass, CO, August 1985.
6. Kaul, U.K., and Chaussee, D.S., "AFWAL Parabolized Navier-Stokes Code: 1983 AFWAL/NASA Merged Baseline Version," AFWAL-TR-83-3118, Informatics General Corporation, Palo Alto, CA, May 1984.
7. Rizk, Y.M., Scott, J.N., and Newman, R.K., "Numerical Simulation of Viscous Supersonic Flows in the Vicinity of Embedded Subsonic or Axially Separated Region," AFWAL-TR-78-3113, University of Dayton Research Institute, Dayton, OH, November 1983.

8. Schiff, L.B. and Steger, J.L., "Numerical Simulation of Steady Supersonic Viscous Flow," AIAA Paper 79-0130, January 1979.

9. Beam, R. and Warming, R.G., "An Implicit Factored Scheme for the Compressible Navier-Stokes Equations," AIAA Journal, Vol. 16, pp. 393-402, April 1978.

10. Chaussee, D.S. and Steger, J.L., "Three-Dimensional Viscous Flow Fluid Program: Part 3, Parabolized Navier-Stokes Program (Interim Report)," AFWAL-TM-81-65-FIMG, Flow Simulations Inc., Sunnyvale, CA, March 1981.

11. Chaussee, D.S., Patterson, J.L., Kutler, P., Pulliam, T., and Steger, J.L., "A Numerical Simulation of Hypersonic Viscous Flows Over Arbitrary Geometries at High Angle of Attack," AIAA Paper 81-0050, January 1981.

12. Neumann, R.O., Patterson, J.L., and Sliski, N.J., "Aerodynamic Heating to the Hypersonic Research Aircraft X-24C," AIAA Paper 78-37, Huntsville, AL, January 1978.

13. Rai, M.M., and Chaussee, D.S., "New Implicit Boundary Procedures: Theory and Applications," AIAA Paper 83-0123, Reno, NV, January 1983.

14. Viegas, J.R. and Horstman, C.C., "Comparison of Multiequation Turbulence Models of Several Shock Separated Boundary-Layer Interaction Flows," AIAA Paper 78-1165, Seattle, WA, July 1978.

15. Lawrence, S.L., Tannehill, J.C., and Chaussee, D.S., "An Upwind Algorithm for the Parabolized Navier-Stokes Equation," AIAA Paper 86-1117, Atlanta, GA, May 1986.

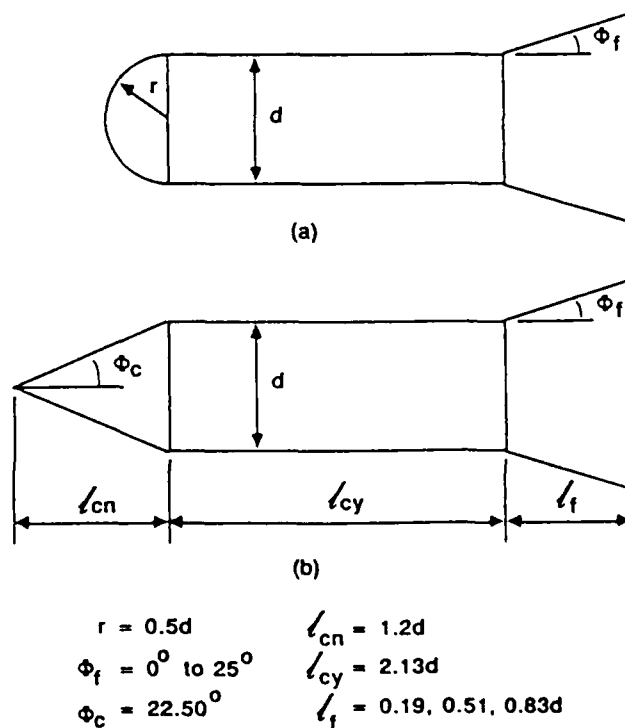


Figure 1. (a) Hemisphere - Cylinder - Flare Geometry
(b) Cone - Cylinder - Flare Geometry

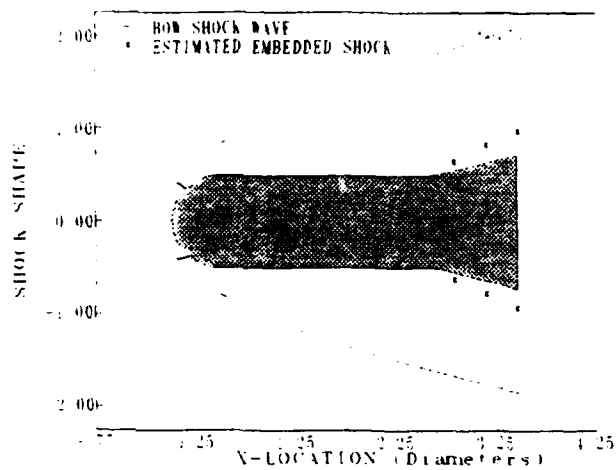


Figure 2. Shock shape of hemisphere-cylinder-flare for 15° flare.

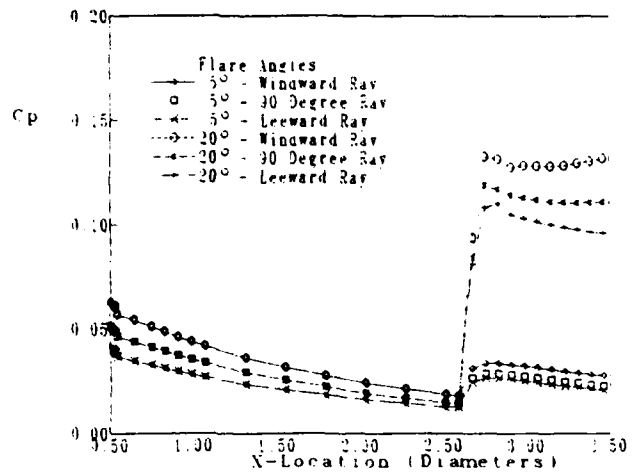


Figure 5. Pressure coefficient distribution for hemisphere-cylinder-flare for 5° and 20° flares.

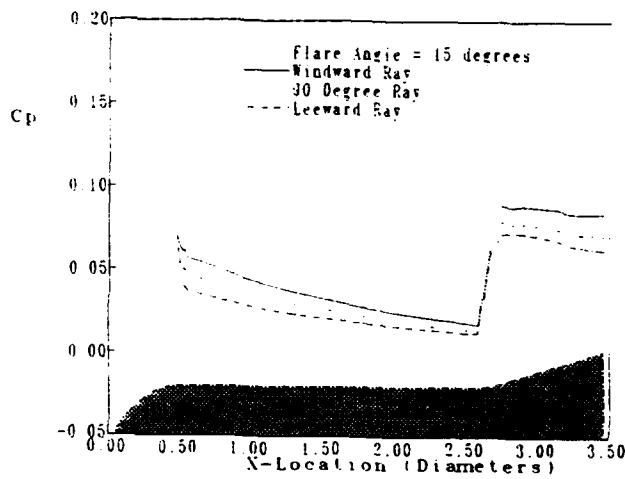


Figure 3. Pressure coefficient distribution for hemisphere-cylinder-flare for 15° flare.

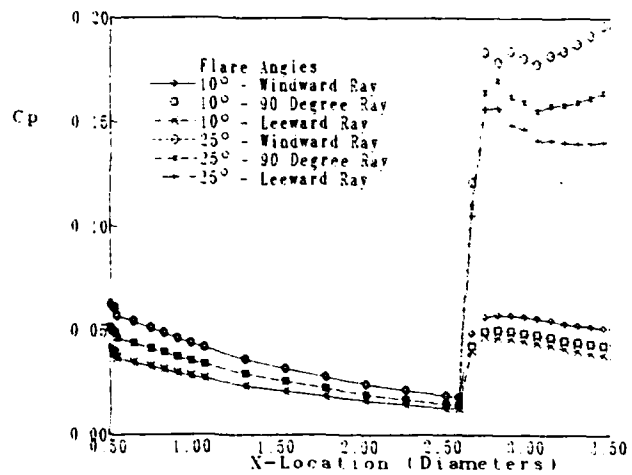


Figure 6. Pressure coefficient distribution for hemisphere-cylinder-flare for 10° and 25° flares.

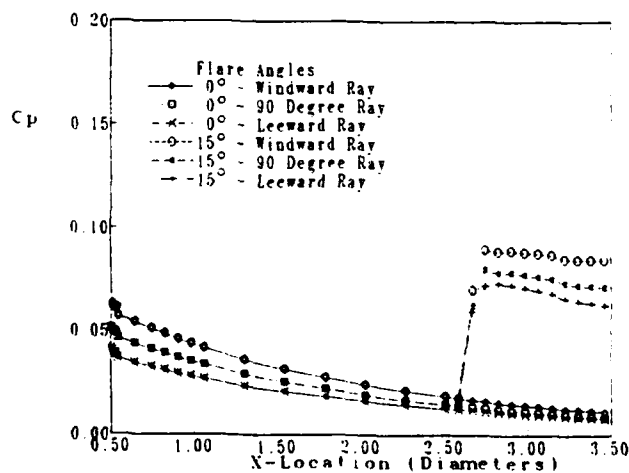


Figure 4. Pressure coefficient distribution for hemisphere-cylinder-flare for 0° and 15° flares.

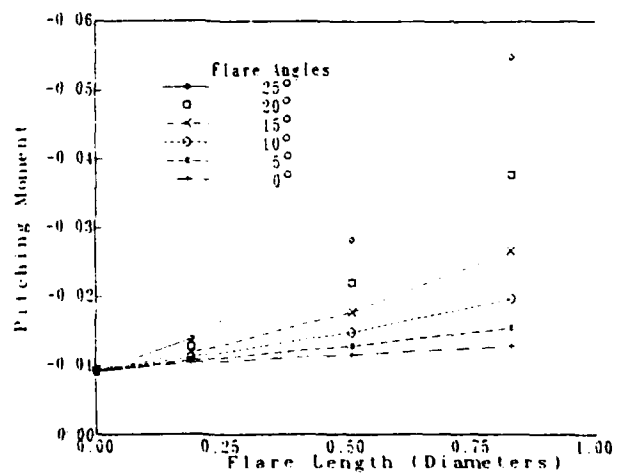


Figure 7. Pitching moment curves for hemisphere-cylinder-flare for 0, 5, 10, 15, 20, and 25 degree flares.

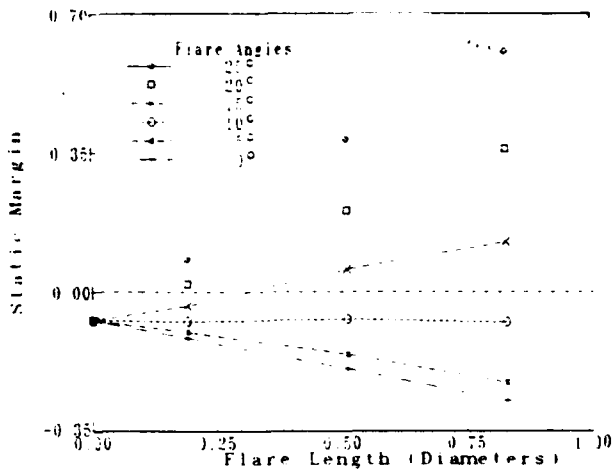


Figure 8. Static margin curves for hemisphere-cylinder-flare for 0, 5, 10, 15, 20, and 25 degree flares.

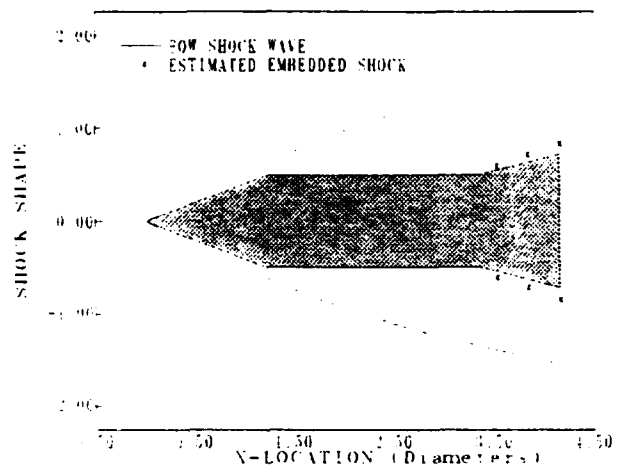


Figure 11. Shock shape for cone-cylinder-flare for 15° flare.

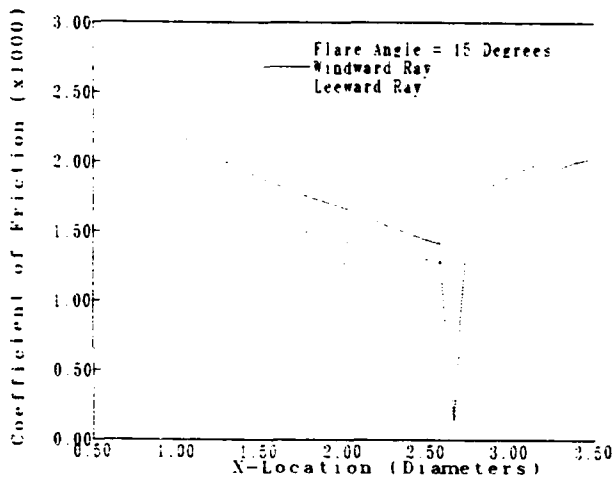


Figure 9. Coefficient of friction curves for hemisphere-cylinder-flare for 15° flare.

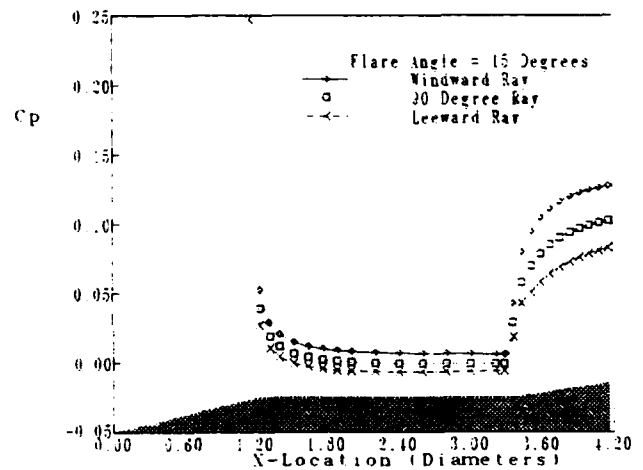


Figure 12. Pressure coefficient distribution for cone-cylinder-flare for 15° flare.

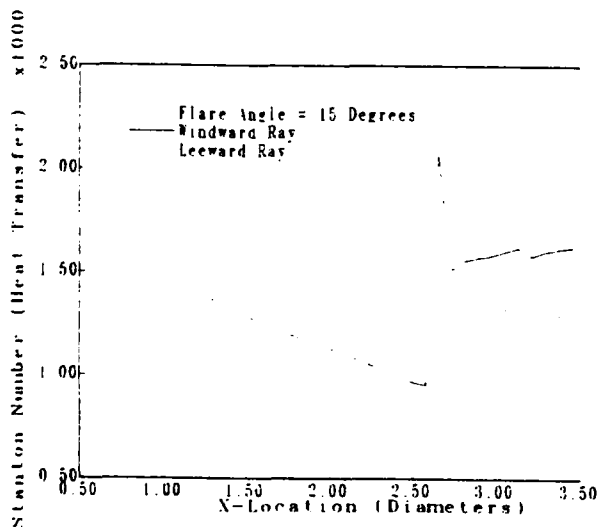


Figure 10. Stanton number (heat transfer) for hemisphere-cylinder-flare for 15° flare.

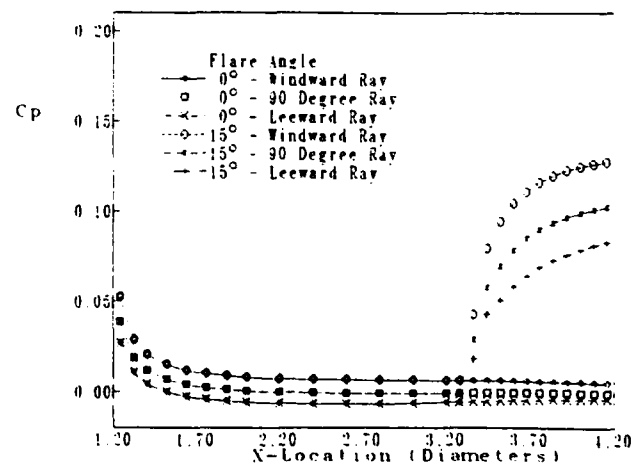


Figure 13. Pressure coefficient distribution for cone-cylinder-flare for 0° and 15° flares.

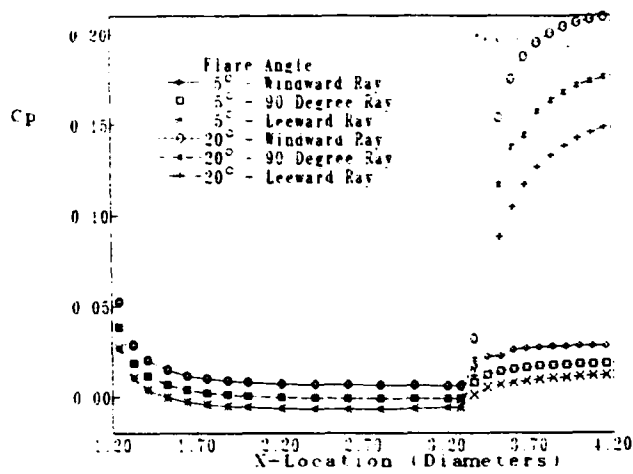


Figure 14. Pressure coefficient distribution for cone-cylinder-flare for 5° and 20° flares.

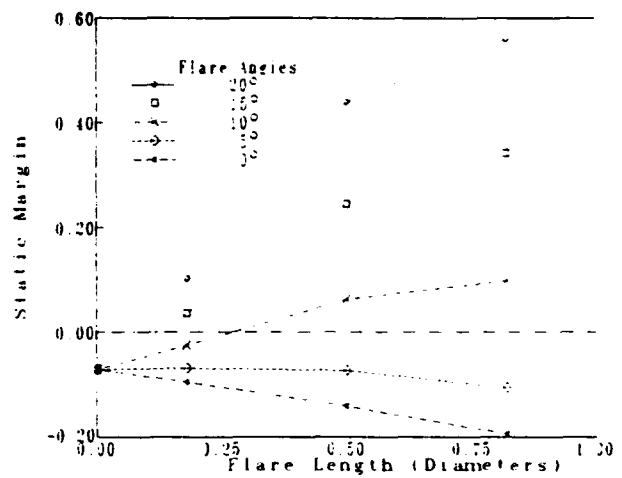


Figure 17. Static margin curves for cone-cylinder-flare for 0, 5, 10, 15, and 20 degree flares.

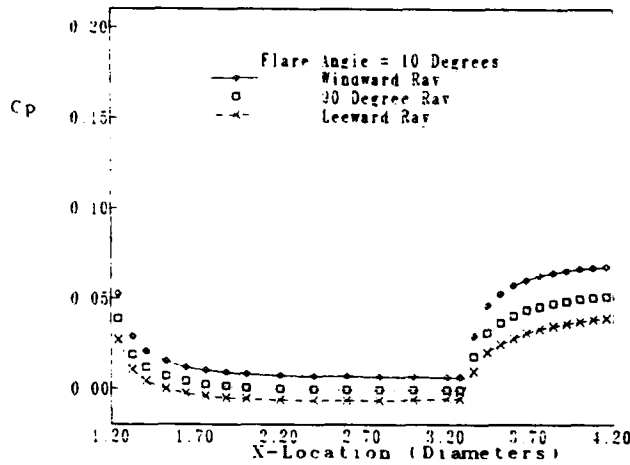


Figure 15. Pressure coefficients distribution for cone-cylinder-flare for 10° flare.

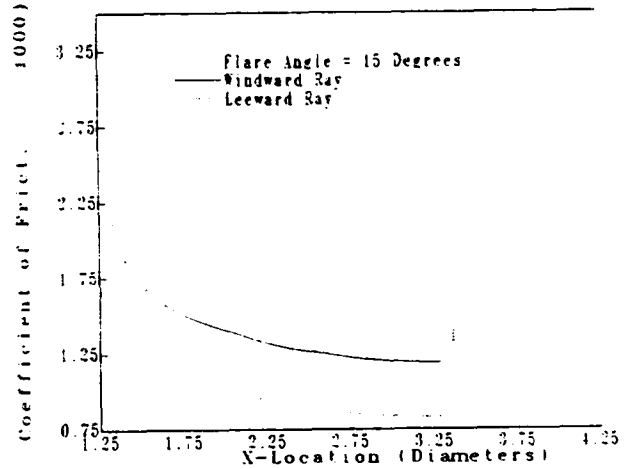


Figure 18. Coefficient of friction curves for cone-cylinder-flare for 15° flare.

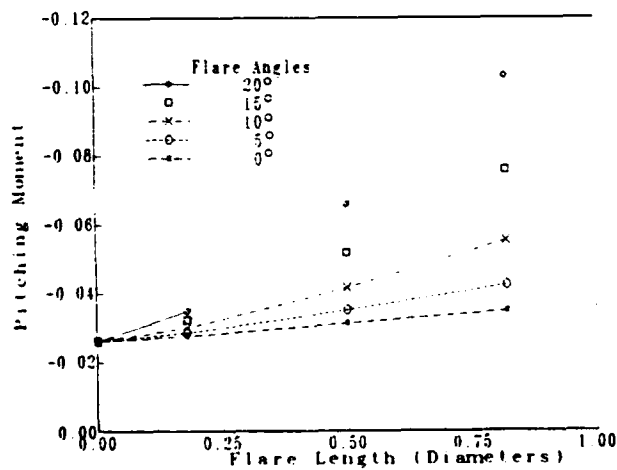


Figure 16. Pitching moment curves for cone-cylinder-flare for 0, 5, 10, 15, and 20 degree flares.

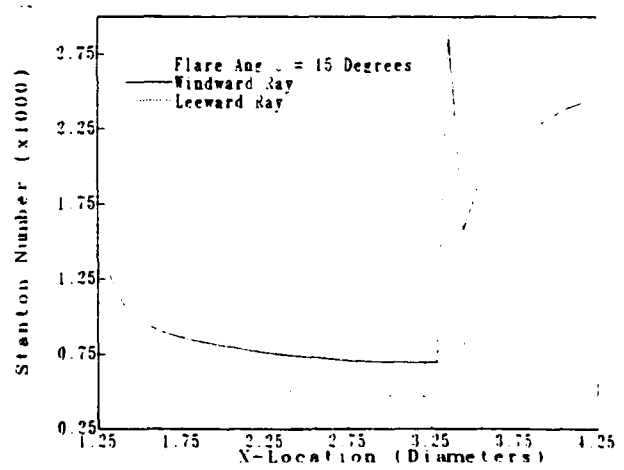


Figure 19. Stanton number (heat transfer) for cone-cylinder-flare for 15° flare.

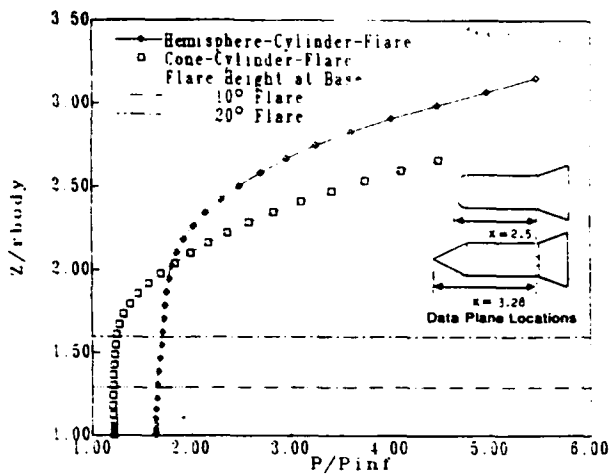


Figure 20. Normalized pressure field comparison at the windward plane.

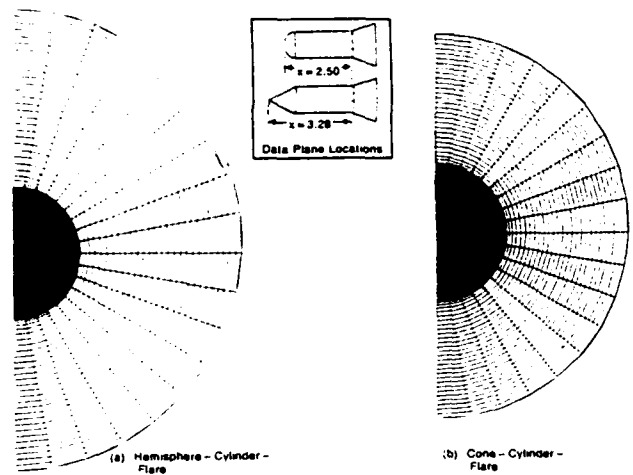


Figure 23. Algebraic grids located at data planes.

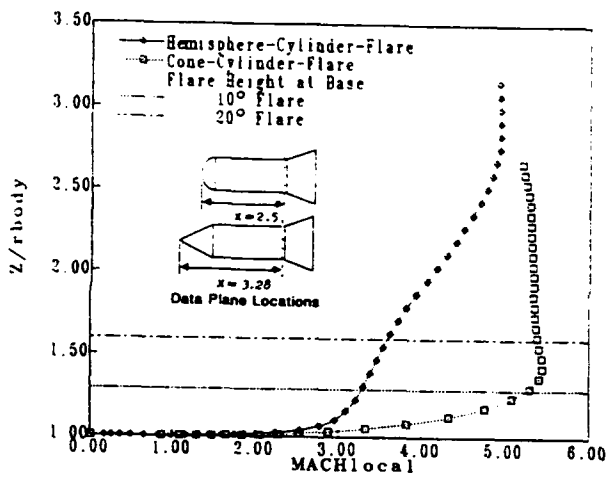


Figure 21. Local Mach number field comparison at the windward plane.

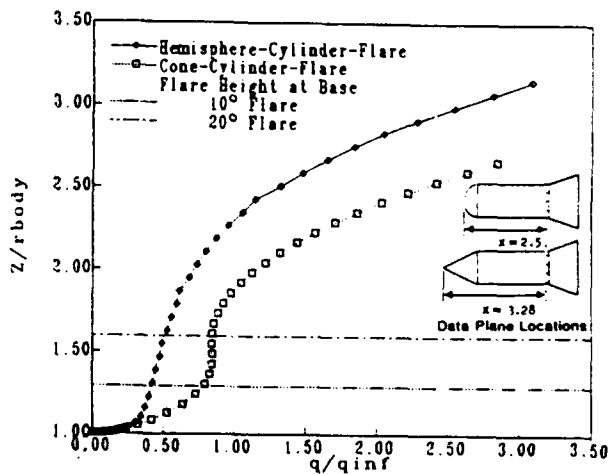


Figure 22. Dynamic pressure field comparison at the windward plane.

END

2-87

DTIC